crystals

MDPI

*Article*

# Exploring Multi-Parameter Effects on Iron Oxide Nanoparticle Synthesis by SAXS Analysis

**Marco Eigenfeld [1,2], Marco Reindl [1], Xiao Sun [3] and Sebastian P. Schwaminger [1,2,*]**

[1] Division of Medicinal Chemistry, Otto Loewi Research Center, Medical University Graz, Neue Stiftingtalstraße 6, 8010 Graz, Austria; marco.eigenfeld@medunigraz.at (M.E.); marco.reindl@medunigraz.at (M.R.)
[2] BioTechMed-Graz, Mozartgasse 12, 8010 Graz, Austria
[3] Deutsches Elektronen-Synchrotron DESY, Notkestraße 85, 22607 Hamburg, Germany; xiao.sun@desy.de
* Correspondence: sebastian.schwaminger@medunigraz.at

**Abstract:** Iron oxide nanoparticles (IONs) are extensively used in biomedical applications due to their unique magnetic properties. This study optimized ION synthesis via the co-precipitation method, exploring the impact of the reactant concentrations (Fe(II) and Fe(III)), NaOH concentration, temperature (30 °C–80 °C), stirring speed (0–1000 rpm), and dosing rate (10–600 s) on particle size and growth. Using small-angle X-ray scattering (SAXS), we observed, for example, that higher temperatures (e.g., 67 °C compared with 53 °C) led to a 50% increase in particle size, while the stirring speed and NaOH concentration also influenced nucleation and aggregation. These results provide comprehensive insights into optimizing synthetic conditions for targeted applications in biomedical fields, such as drug delivery and magnetic resonance imaging (MRI), where precise control over nanoparticle size and properties is crucial.

**Keywords:** iron oxide nanoparticles; small-angle X-ray scattering; nanoparticle synthesis; nanoparticle size; nucleation and growth dynamics; biomedical applications; aggregation behavior



**Citation:** Eigenfeld, M.; Reindl, M.; Sun, X.; Schwaminger, S.P. Exploring Multi-Parameter Effects on Iron Oxide Nanoparticle Synthesis by SAXS Analysis. *Crystals* **2024**, *14*, 961. https://doi.org/10.3390/cryst14110961

Academic Editors: Rajratan Basu and Vladimir I. Zverev

Received: 9 October 2024
Revised: 19 October 2024
Accepted: 3 November 2024
Published: 4 November 2024



## 1. Introduction

The field of nanomedicine is continuously evolving, driven by the development of innovative materials that enhance diagnostic and therapeutic technologies. Iron oxide nanoparticles (IONs) exemplify this innovation, known for their superparamagnetic properties, minimal toxicity, and high surface-to-volume ratio [1–3]. These unique characteristics make IONs particularly effective in treating and diagnosing diseases such as cancer.

In oncology, IONs are utilized for both therapeutic and diagnostic purposes. They enhance magnetic resonance imaging (MRI) as T2 contrast agents, providing clearer delineation of anatomical structures and enabling more accurate diagnoses, such as detecting small tumors in preclinical models like mice [4–7]. IONs are also used in targeted drug delivery and magnetic hyperthermia therapy, where they accumulate in tumor tissues and generate heat in response to external magnetic fields, selectively destroying cancer cells while minimizing damage to healthy tissue [8–11].

IONs are typically synthesized using the co-precipitation method, which is favored for its speed and cost-effectiveness [12,13]. This method produces magnetically responsive particles that can be easily manipulated by magnetic fields, making them ideal for applications in both imaging and therapy. A key aspect of our research focused on exploring the kinetics of ION formation through this synthetic process, aiming to optimize their use in medical applications [14–17] since nanoparticles' morphology (e.g., nanoflowers, rod-shaped, or cubic) determines their interconnections by influencing properties like alignment, aggregation, stability, and magnetic behavior, which are critical in applications such as hyperthermia and magnetic sensing [18,19].

To deepen our understanding of IONs and their potential applications, it is important to examine both the synthetic methods and characterization techniques employed in their development. Several synthetic routes, such as thermal decomposition [20,21], hydrothermal synthesis [21], and sol–gel methods [22], offer varying degrees of control over particle size, shape, and crystallinity. Thermal decomposition, while offering better control over particle size and crystallinity, often leads to structural defects and polycrystallinity, reducing magnetic properties [23]. Additionally, the formation of nonmagnetic phases like wüstite in oxygen-deficient conditions further limits performance unless post-synthetic oxidation is applied, making it less ideal for producing highly magnetic nanoparticles [23]. Hydrothermal synthesis produces high-quality particles but often results in inconsistent sizes, requires longer reaction times, and operates at high pressures, making scaling up and cost-effectiveness challenging compared with co-precipitation [24].

The co-precipitation method is widely favored due to its speed and cost-efficiency [13,25,26]. This method involves the simultaneous precipitation of ferrous and ferric ions in an alkaline medium, producing nanoparticles with desirable magnetic properties for subsequent applications, such as imaging and therapy.

To thoroughly investigate nanoparticle properties, it is crucial to employ advanced characterization techniques that provide comprehensive insights into particles' size, shape, and distribution, especially very detailed during and after processes, such as Ostwald ripening [27,28]. Understanding these characteristics enables the optimization of IONs for specific diagnostic and therapeutic applications. For example, in cell separation, agglomerated particles are preferred over single particles [29]. In contrast, for drug delivery, maintaining a strict particle size is crucial to ensure both efficacy and safety [30], as a consistent particle size is the key to reproducible results.

Small-angle X-ray scattering (SAXS) has been extensively used to characterize nanoparticles produced by co-precipitation. This technique is particularly valuable for understanding the early stages of nanoparticle formation, including particle seeding and growth kinetics. SAXS is sensitive to variations in electron density and can provide detailed information on particles' size, shape, and distribution, making it ideal for studying the dynamics of nanoparticle synthesis. For instance, studies have utilized in-situ SAXS experiments to monitor the formation of IONs in real time, revealing the rapid formation of primary nanoparticles and their subsequent aggregation into larger structures [31].

In the context of co-precipitation, SAXS has been employed to elucidate the mechanisms of ION formation under different conditions. For example, in a gas/liquid mixed-phase fluidic reactor, SAXS measurements helped clarify how the reaction time, pH, and valence state of iron ions affected the formation of nanoparticles. It was observed that at higher pH levels, the rapid precipitation and aggregation of primary particles led to the formation of $Fe_3O_4$ nanoparticles within minutes [31]. Similarly, in situ SAXS has been used to study the impact of quick mixing modes in co-precipitation, demonstrating how rapid and homogeneous mixing can prevent the formation of intermediate crystalline phases, thereby streamlining the synthetic process [26].

These insights highlight the critical role of SAXS in advancing our understanding of nanoparticle synthesis, particularly in optimizing the conditions for producing IONs with desirable properties for medical applications.

We employed SAXS, a technique that quantifies the elastic scattering of X-rays at small angles, to derive information regarding the size, shape, and distribution of particles within the nanometer scale [32]. In situ SAXS is a powerful tool for the real-time monitoring of nanoparticle growth, from initial seed formation to the mature phase. This technique facilitates the observation of nanoparticle evolution, providing insights into the dynamics of nanoparticle formation and growth mechanisms, such as Ostwald ripening, a process where larger particles grow at the expense of smaller ones, influenced by solubility gradients.

This investigation delved into the synthetic parameters that influence the characteristics of IONs, such as size, magnetization, and chemical composition. By systematically investigating these properties and monitoring their evolution over time using SAXS, we

provide a detailed analysis of how the synthetic process unfolds. This approach allows us to understand how nucleation and growth are also influenced by time, offering valuable insights into the optimal duration of synthesis. Unlike earlier studies that focused solely on endpoint analyses, our research captures the dynamic changes during the process. Building on foundational research, we seek to expand our knowledge of the potential and adaptability of IONs, advancing their application in both diagnostic and therapeutic modalities in medicine.

## 2. Materials and Methods

### *2.1. Instrument Settings*

Combined small- and wide-angle X-ray scattering (SAXS/WAXS) experiments were performed at the SAXSMAT beamline P62 at DESY (Deutsches Elektronen-Synchrotron), Hamburg, Germany, at a beam energy of 12 keV [33]. For the experiments, the samples were reacted in a small glass beaker at different temperatures according to the respective conditions. The suspensions were continuously pumped through a 3 mm glass capillary, where the samples were measured every 5 s using combined SAXS/WAXS techniques. The SAXS patterns were recorded using an Eiger2X 9M detector, and an Eiger2X 4M was used for WAXS. The sample-to-detector distance was calibrated to be 1.966 m for SAXS and 0.277 m for WAXS. A schematic representation is given in Figure 1.

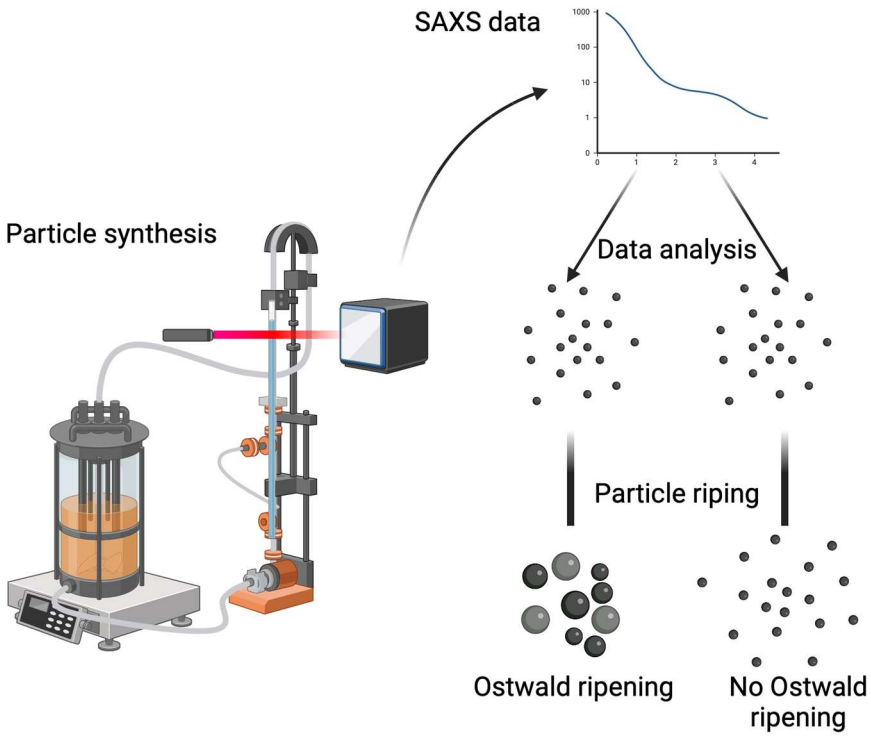


**Figure 1.** A schematic illustration of the experimental setup and potential outcomes.

### *2.2. Synthetic Parameters*

Ferrous and ferric chloride were used as Fe(III)$Cl_3 \cdot 6H_2O$ and Fe(II)$Cl_2 \cdot 4H_2O$, respectively. As specified in Table 1, these salts were weighed and dissolved in 20 mL of deionized and degassed water. Sodium hydroxide was dissolved in 100 mL of deionized and degassed water, resulting in a total reaction volume of 140 mL for each experiment.

**Table 1.** Parameters for experimental planning.

| Parameter | −1 | 0 | 1 |
|---|---|---|---|
| A: Iron(II)chloride in g | 0.35 | | 0.7 |
| B: Iron(III)chloride in g | 0.519 | | 1.037 |
| C: Sodium hydroxide in g | 0.72 | | 1.44 |
| D: Temperature T in °C | 30 | 55 | 80 |
| E: Stirring speed in rpm | 0 | 500 | 1000 |
| F: Dosing rate in s | 10 | 30 | 600 |

The sodium hydroxide solution was stirred with a magnetic stirrer in a glass beaker. Before adding the iron chloride solutions, the reaction temperature was adjusted and maintained. The solutions were added at controlled dosing speeds. For experiments with long reaction times at high temperatures, the reaction volume was kept constant by adding deionized and degassed water. Each reaction was conducted for 100 min.

Experiments were carried out under varying conditions to assess the impact of the temperature and stirring speed on the reaction. Specifically, reactions were performed at three different temperatures (20 °C, 55 °C, and 80 °C) and at three different stirring speeds (0, 500, and 1000 rpm).

### *2.3. SAXS Data Analysis*

The small-angle X-ray scattering (SAXS) data were processed and analyzed using R and Python. The analysis involved several key steps to understand the structural behavior of the complex materials.

#### 2.3.1. Guinier Region Analysis

The code identified the linear Guinier region ($q < 1/R_g$) by computing the first derivative of the scattering intensity, log(I(q)), with respect to the scattering vector, log(q). A sixth-degree polynomial was fitted to this derivative to identify inflection points, which indicated changes in the curvature of the scattering data. These inflection points indicated transitions in particle size, shape, and aggregation phenomena, offering insights into the material's structure under various conditions, and were denoted as $q*$. The hydrodynamic diameter of a particle was calculated based on:

$$R_G = \frac{1}{q^*}; \qquad R_h = \frac{1}{q^*} \cdot \sqrt{\frac{5}{3}} \qquad \text{and} \qquad d_h = 2 \cdot R_h$$

where $R_G$ is the radius of gyration; $R_h$ is the hydrodynamic radius; and $d_h$ is the hydrodynamic diameter.

#### 2.3.2. Starting Point

The analysis focused on identifying key points in the scattering data related to particle aggregation dynamics. This included calculating the mean of the first 5 points of the lowest q at the beginning of the measurement, which indicated the presence of single particles and small aggregations, as well as the slope and endpoint of aggregation, defined as the measurement endpoint after 6000 s.

#### 2.3.3. Slope Analysis

The synthesis speed was determined by the slope analysis of particle size increases using LOESS (locally estimated scatterplot smoothing) [34] fitting and Savitzky–Golay filtering. LOESS provided a smooth representation of the intensity changes over time by modeling the data's underlying trend without assuming a specific parametric form. The Savitzky–Golay filter, a digital smoothing polynomial filter, enhanced the trend detection by preserving higher-moment features like peaks and troughs [35]. Both filter methods

were applied to each dataset, and their effectiveness was manually compared to determine the best approach for each case.

#### 2.3.4. Endpoint Calculation

The endpoint (threshold) for each synthesis was determined by using a rolling median to identify a stable region. This was realized by locating areas with minimal variance, such as regions where the Ostwald ripening trend became limited or reached a steady state.

#### 2.3.5. Response Surface Methodology (RSM)

All identified data points were used in a response surface methodology (RSM) model to calculate the significant parameters influencing three key factors: the minimal particle diameter (starting point), synthesis speed (slope analysis), and aggregation diameter after 10 min (endpoint calculation). The formula for the RSM was:

$$y = \beta_0 + \sum_{i=1}^{k} \beta_i x_i + \sum_{i=1}^{k} \beta_{ii} x_i^2 + \sum_{i<j} \beta_{ij} x_i x_j + \varepsilon$$

Outliers were identified using Cook's distance, with the threshold set at 4/numbers of observations.

### *2.4. WAXS Data Analysis*

WAXS analysis was performed by plotting q versus I(q) for all data points in each experimental setup and calculating the q-value and corresponding intensity I(q) at the maximum. The mean and standard deviation of all 1200 values per measurement were then calculated and compared across all experiments.

## 3. Results and Discussion

WAXS analysis confirmed the presence of crystallinity from the beginning of synthesis (Figures A1 and A2; Appendix A). The analysis of the I(q)- and q-values indicated that the crystallinity was consistent and well-defined across most of the datasets. The average intensity, I(q), remained stable between 1500 and 1600, with low standard deviations, indicating uniform scattering properties and a homogeneous crystalline structure throughout the samples. Additionally, the q-values, corresponding to the interplanar distances, were consistently around 2 $Å^{-1}$, confirming stable interplanar spacing in the crystalline regions. These observations suggest uniform and well-maintained crystallinity across the majority of the samples, with minimal variations in both the scattering intensity and structural periodicity.

The structural characteristics and aggregation dynamics of particles were evaluated with SAXS measurements. In Figure A3 in Appendix A, a comparison of the Guinier plots for Dataset 3 at the first and last measurement points is shown. In the Guinier plots for 5 s and 600 s (10 min), we observed differences in the Guinier region (the linear region at low $q^2$-values). The steeper slope in this region at 5 s suggests that the particles in this dataset were smaller than those at 600 s, as the slope of the Guinier plot is inversely related to the radius of gyration ($R_g$). At 600 s, the Guinier region extended over a larger range of $q^2$-values, indicating that the probed structure had a broader distribution of scattering particles or potentially larger particles.

For further evaluation, the inflection points in the Guinier region were evaluated.

The scatter plot in Figure 2 illustrates the change in the particle diameter over time for the two datasets conducted under different experimental conditions. Dataset 4 was characterized by low iron salt concentrations (0.35 g ($Fe(II)Cl_2$) and 0.519 g ($Fe(III)Cl_3$)), a temperature of 53 °C, a stirring speed of 860 rpm, and a moderate dosing rate of 266.65 µL/min. In contrast, Dataset 3 was obtained at a higher temperature of 67 °C and a slower stirring speed of 136 rpm, with a comparable dosing rate of 211.35 µL/min. The salt concentrations in Dataset 3 were higher, at 0.534 g and 1.037 g.

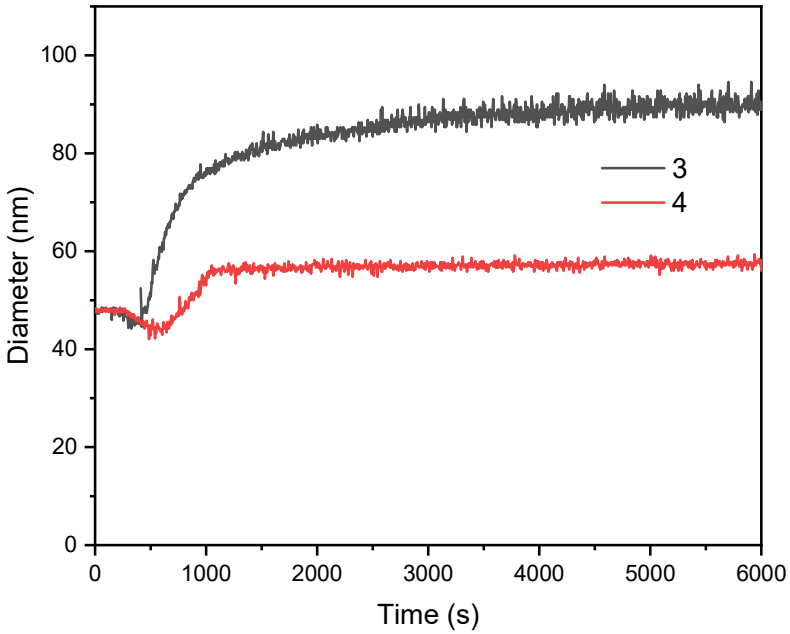


**Figure 2.** Changes in particle hydrodynamic diameter over time for two different synthesis methods for Dataset 3 and Dataset 4. Dataset 4 featured low iron salt concentrations (0.35 g and 0.519 g), a temperature of 53 °C, stirring at 860 rpm, and a dosing rate of 266.65 µL/min. Conversely, Dataset 3 had higher salt concentrations (0.534 g and 1.037 g) and was recorded at 67 °C with a slower stirring speed of 136 rpm and a similar dosing rate of 211.35 µL/min. Datapoints per synthesis = 1.200.

The differences in these conditions—particularly temperature, stirring speed, and salt concentration—highlighted their impacts on the kinetics of particle growth, including the synthesis speed, final particle diameter, and Ostwald ripening [36]. Ostwald ripening, a process where larger particles grow at the expense of smaller ones, was more prominent in Dataset 3 due to the longer time taken to reach a stable particle diameter. In contrast with the detailed measurement of particle formation, it can be seen that Dataset 4 reached a stable particle diameter more quickly, therefore indicating that the synthesis could be stopped earlier. The scatter plot visually captures these dynamics, demonstrating how variations in the experimental parameters can lead to significant changes in particle size evolution over time.

TEM analysis revealed predominantly cubic nanoparticles, with sizes ranging from 10 to 25 nm for individual particles. However, due to differences in the sample preparation, the agglomeration observed in SAXS could not be replicated in TEM. The cubic, hexagonal, and spherical shapes of the nanoparticles synthesized by co-precipitation resulted from the balanced growth of crystal facets under the reaction conditions, such as pH and temperature, and the absence of anisotropic growth drivers or shape-directing agents that would promote more complex forms like rods or nanoflowers [37].

XRD data were evaluated earlier by Schwaminger et al. to identify the phase of iron oxide nanoparticles [13].

### *3.1. RSM Analysis of Starting Point*

To explore the relationships between the predictors—(A) Fe(III), (B) Fe(II) salts, (C) sodium hydroxide amount, (D) temperature, (E) stirring rate, and (F) dose rate—and the response variable of particle size during and after synthesis, the RSM (response surface methodology) was applied to the start of particle formation using the mean of the first five data points. The mean of the lowest stable initial values in the SAXS data was calculated by averaging the reciprocal values of the first five inflection points. This provided a direct measurement of the initial particle size at the beginning of synthesis.

The ordinary least squares (OLS) regression analysis revealed a strong model fit between the radius of gyration and the predictors A–F, with an R-squared value of 0.919 and an adjusted R-squared value of 0.730, indicating that 91.9% of the variance in the dependent variable was explained by the model.

In the context of magnetic nanoparticle synthesis, the RSM regression analysis identified several key factors that influence particle size. Variable B, representing Fe(III), had a positive coefficient of 435.4094. This indicates that an increasing concentration of Fe(III) leads to larger particle sizes. This suggests that Fe(III) plays a crucial role in enhancing the nanoparticle growth process, potentially due to its involvement in the nucleation and particle formation mechanisms, which aligns with the literature [38]. The availability of Fe(III) ions may facilitate the formation of larger nanoparticles by providing more material for growth [13,39].

Variable C, which represented sodium hydroxide, showed an even more pronounced positive effect, with a coefficient of 569.6892, especially when interacting with temperature, variable D ($p$ = 0.312) (Figure 3). This emphasizes the critical contribution of temperature to increasing particle size. Sodium hydroxide likely acts as a key driver in the synthetic process by controlling the pH, which can affect the rate of hydrolysis and precipitation of iron ions. The literature emphasizes that the alkaline environment provided by sodium hydroxide is essential for achieving a high degree of supersaturation, which is necessary for the nucleation and subsequent growth of nanoparticles [13]. Also, in other co-precipitation processes, the observation that higher alkaline molarities result in higher particle sizes has been made [40]. As seen in Figure 2, at high temperatures and high NaOH concentrations, the nucleation rate of IONs can increase. The rapid growth of the particles can lead to quicker aggregation into larger clusters. The study by Siregar et al. [41] demonstrated that varying the NaOH concentrations from 0.5 M to 6 M and synthesis temperatures from 30 °C to 120 °C significantly affected the microstructural and magnetic properties of $Mn_{0.5}Zn_{0.5}Fe_2O_4$ nanoparticles, indicating that such conditions can influence the nucleation rate and growth dynamics of IONs. Another study highlighted that superparamagnetic IONs require NaOH concentrations above a critical threshold, with both particle size and magnetic properties being significantly influenced by stirring rates during co-precipitation, underscoring the importance of synthesis parameters in controlling nanoparticle characteristics [42].

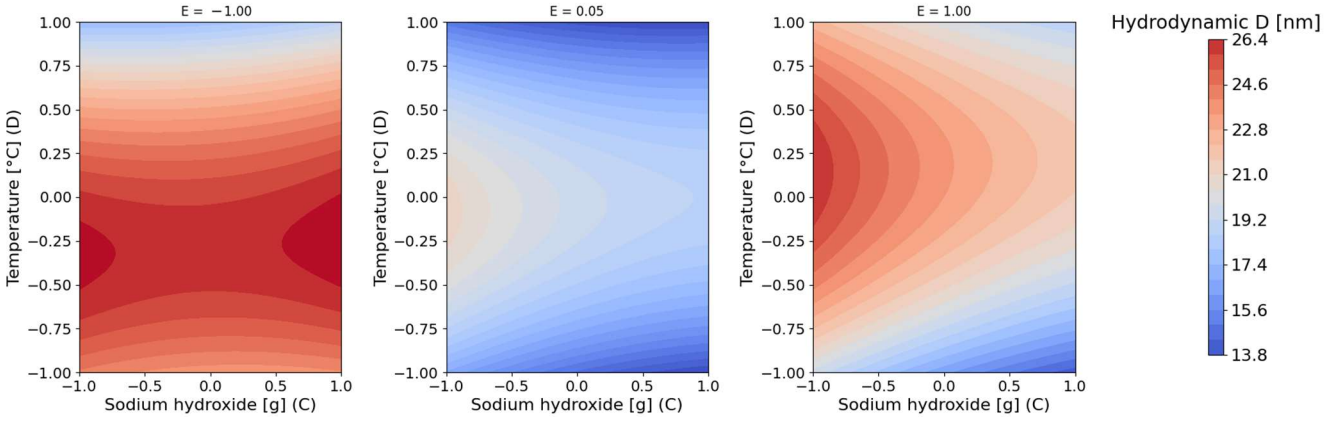


**Figure 3.** Contour plot depicting the impact of sodium hydroxide amount (−1:0.72 g; 1:1.44 g) and temperature (−1:30 °C; 1:80 °C) on the hydrodynamic diameter, indicated in nanometers by different stirring speeds (E = −1:0 rpm; E = 1:1000 rpm).

However, the significance of the synthesis parameters on the initial particle formation was generally low, with only a significant quadratic effect for temperature ($p$ = 0.013). One study from the literature observed that a decrease in the synthesis temperature leads to increased crystallinity and larger nanoparticle size while maintaining a $Fe^{2+}$–$Fe^{3+}$ molar ratio of 1:2 with 0.4 M NaOH [43]. It should be noted that in our observations, this applied

only to the initial nucleation, not to the overall particle growth. All other parameters did not show a significant impact on the synthesis at a significance level of $p < 0.05$.

### *3.2. RSM Analysis of Slope*

To analyze the particle growth rate and the impact of parameters A–F on the growth speed, we examined the slopes of the time to the inflection point graph (Figure 4).

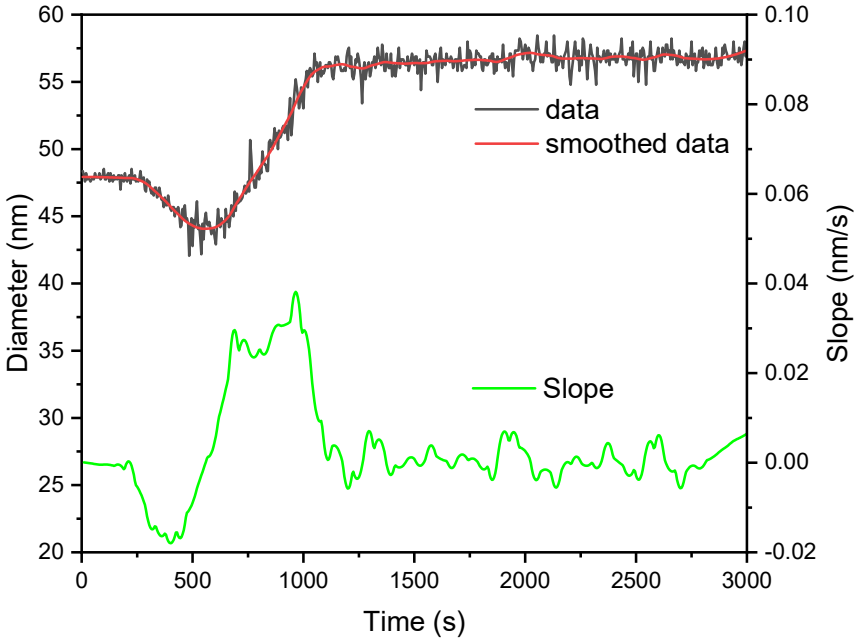


**Figure 4.** Analysis of maximum slope, corresponding to the particle growth rate of Dataset 4. Dataset 4: salt concentrations of 0.35 g and 0.519 g, temperature of 53 °C, stirring speed of 860 rpm, and dosing rate of 266.65 µL/min. Grey: measurement data of hydrodynamic diameter; red: smoothed data; green: smoothed slope of measurement data.

The RSM regression analysis mentioned above for the slope of the growth rate indicated a strong model fit, with an R-squared value of 0.967, showing that 96.7% (adj. R-squared: 0.840) of the variance in the growth rate was explained by the model.

The analysis revealed that the interaction between the Fe(II) (A) and Fe(III) amounts (B) significantly impacted the growth rate, with a coefficient of −0.2818 ($p = 0.024$) (Figure 5). While both Fe(II) and Fe(III) individually contributed positively to the growth process, their combined increase resulted in a decreased growth rate. This negative interaction might be due to the formation of larger particles or aggregates, which could slow down the overall growth dynamics [44].

In contrast, the interaction between the Fe(II) mass (A) and sodium hydroxide (C) showed a significant positive effect on the growth rate, with a coefficient of 0.2387 ($p = 0.021$). Higher concentrations of Fe(III) coupled with elevated temperatures appeared to accelerate growth. This likely resulted from the enhanced kinetic energy and reaction rates that facilitated particle nucleation and growth.

However, the interaction between sodium hydroxide (C) and the stirring rate (E) was significant, with a negative coefficient of −0.1711 ($p = 0.026$). While an increased temperature generally promotes growth, excessive stirring may counteract this effect by potentially breaking up aggregates, thereby reducing the overall growth rate.

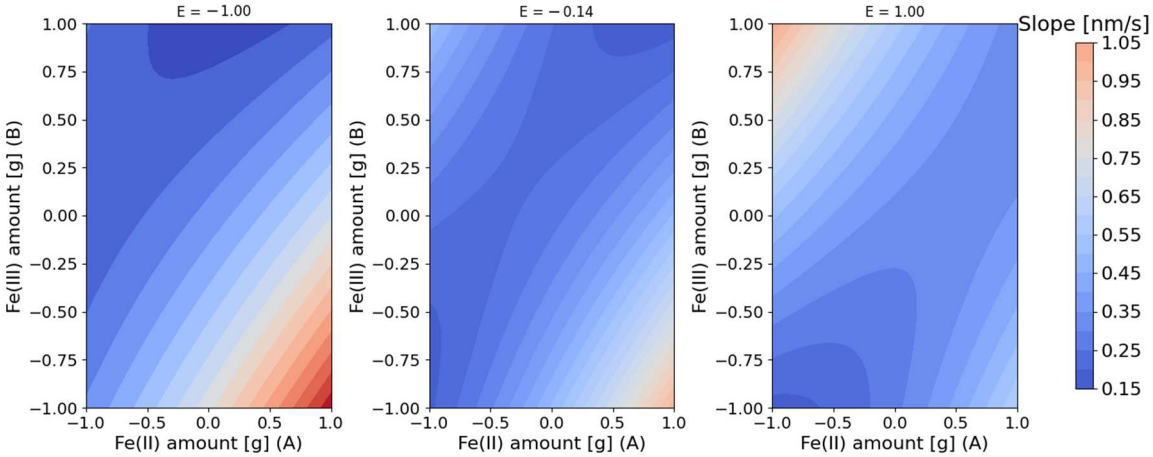


**Figure 5.** Contour plot showing the relationship between Fe(II) and Fe(III) amounts and the slope, indicating the speed of agglomeration formation by different stirring speeds (E = 0:0 rpm; E = 1:1000 rpm).

### *3.3. RSM Analysis of the Endpoint Particle Size*

The R-squared value of 0.939 indicated that 93.9% of the variance in the response variable was explained by the model. The adjusted R-squared value was 0.735, suggesting a good model fit even after accounting for the number of predictors. The F-statistic was 4.589 with a *p*-value of 0.0153, indicating that the overall model was statistically significant. The significant factors in the model with *p*-values of less than 0.05 were temperature (D), the interaction between Fe(II) and Fe(III) (A–B); the interaction between Fe(II) and the stirring speed (A–E); and the interaction between the temperature and the stirring speed (D–E). Lastly, the sodium hydroxide term had a quadratic effect ($I(C^2)$).

The temperature (D) ($p < 0.001$) positively influenced the aggregation size, with a unit increase in D leading to an increase in the particle size, indicating bigger aggregation sizes (Figure 6). This is supported by Qu et al. [45], who demonstrated that higher reaction temperatures lead to an increase in cobalt ferrite nanoparticles' size. Similarly, Siregar et al. [41] confirmed this trend, showing that crystallite sizes grew from 14.1 nm to 26.7 nm as the temperature increased. Conversely, as mentioned earlier, it has been observed in a study that a decrease in the synthesis temperature leads to increased crystallinity and a larger nanoparticle size while maintaining a $Fe^{2+}$–$Fe^{3+}$ molar ratio of 1:2 with 0.4 M NaOH [43]. The conditions were not exactly the same as seen in the other mentioned studies due to the use of higher NaOH concentrations and the type of nanoparticles. Therefore, the observations cannot be directly compared but should still be taken into account for interpretation.

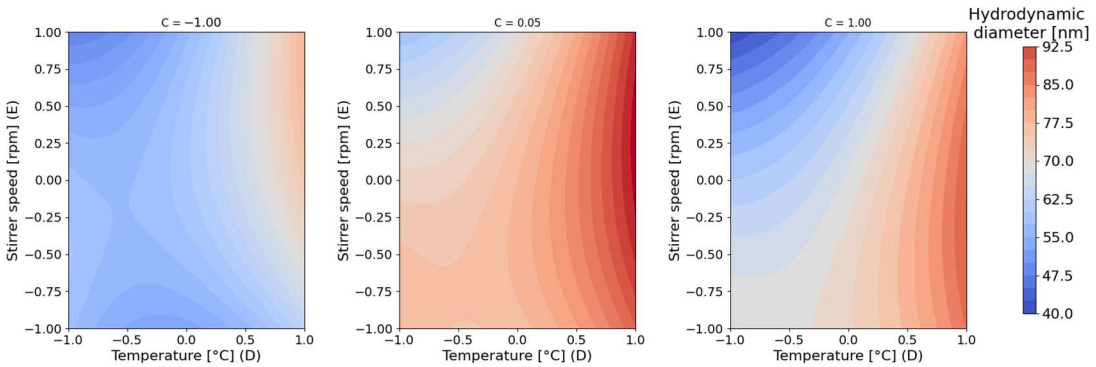


**Figure 6.** Contour plots illustrating interaction between temperature and stirrer speed at varying sodium hydroxide concentrations (C = −1:0.72 g; C = 1:1.44 g) toward hydrodynamic diameter.

The analysis indicated that the final aggregate diameters were influenced by a complex interplay of factors. Higher temperatures (D) consistently enhanced growth, likely due to increased reaction kinetics [31]. The interactions between the Fe(II) concentration (A) and both the Fe(III) concentration (B) and stirring rate (E) suggested synergistic effects that boosted aggregate size. However, the negative interaction between sodium hydroxide (C) and the stirring rate (E), along with the significant negative quadratic effect of temperature, suggested that excessive temperatures can hinder growth, pointing to an optimal temperature range for synthesis. Besenhard discussed the use of in situ SAXS for understanding nanoparticle formation kinetics [26]. He noted that the concentration ratios and stirring rates affect the nucleation and growth rates, which subsequently influence the final particle size and distribution [26], supporting our findings.

Our observations reveal that adding NaOH to increase pH accelerates nucleation but can lead to uneven nanoparticle growth unless properly mixed. This interaction between sodium hydroxide concentrations and stirring rates suggests that maintaining an optimal balance is crucial to prevent excessive aggregation or the formation of unwanted phases, aligning with the literature findings [26,31]. This hypothesis is further supported by the findings of the study conducted by Wicaksono et al. [46], which showed that fine-tuning the Fe(II)/Fe(III) ratio can significantly enhance control over the synthetic process and improve the magnetic properties of nanoparticles. Additionally, the research by Mona et al. [47] demonstrates that variations in temperature and precursor concentrations impact the morphological and structural characteristics of IONs, with higher temperatures inducing phase transitions and influencing particle size. These insights collectively emphasize the importance of meticulously controlled synthetic conditions to achieve specific nanoparticle characteristics.

## 4. Conclusions

This study demonstrates the significant roles of temperature, sodium hydroxide concentration, and stirring speed in the synthesis and growth of IONs. The initial particle size is reduced by temperature, but when combined with higher stirring speeds, the final particle diameter is increased. Elevated temperatures and higher concentrations of sodium hydroxide markedly increase particle size through accelerated reaction kinetics and nucleation. The ratios of iron(II) chloride, iron(III) chloride, and sodium hydroxide significantly influence particle growth and final size. While increased stirring speeds enhance particle growth by improving mixing and mass transfer, overly vigorous stirring can disrupt aggregate formation and hinder Ostwald ripening. Additionally, the dosing rate decreases particle growth. The growth and final particle diameter results are consistent with earlier findings [13,38], whereas the initial particle diameter results are less significant and contrast with recent studies. In summary, our findings underscore the necessity of meticulously optimizing synthetic conditions to finely tune the nanoparticle size and achieve uniformity in production. The precise control of experimental parameters is essential for tailoring nanoparticle characteristics to meet specific application needs, highlighting the delicate balance between promoting growth and maintaining the desired particle structure. Future studies could focus on applying these insights to scalable industrial processes, ensuring consistent nanoparticle quality, exploring the role of these parameters in tailoring nanoparticles for advanced applications, such as drug delivery and catalysis, and investigating the potential cytotoxic effects of these particles to ensure their safety in biomedical applications.

**Author Contributions:** Conceptualization, M.R. and S.P.S.; methodology, M.R. and S.P.S.; validation, M.E. and S.P.S.; data curation, M.E., X.S. and S.P.S.; writing—original draft preparation, M.E.; writing—review and editing, M.E., M.R., X.S. and S.P.S.; visualization, M.E.; supervision, S.P.S.; project administration, S.P.S.; funding acquisition, S.P.S. All authors have read and agreed to the published version of the manuscript.

**Funding:** This research was funded by the MEFO Graz. Marco Reindl was trained within the frame of the PhD program in Molecular Medicine.

**Data Availability Statement:** The data presented in this study are available upon reasonable request from the authors.

**Conflicts of Interest:** Authors Marco Eigenfeld and Sebastian P. Schwaminger were employed by BioTechMed-Graz, the remaining authors declare that the research was conducted in the absence of any commercial or financial relationships that could be construed as a potential conflict of interest.

## Appendix A

*Appendix A.1. WAXS Data Plots*

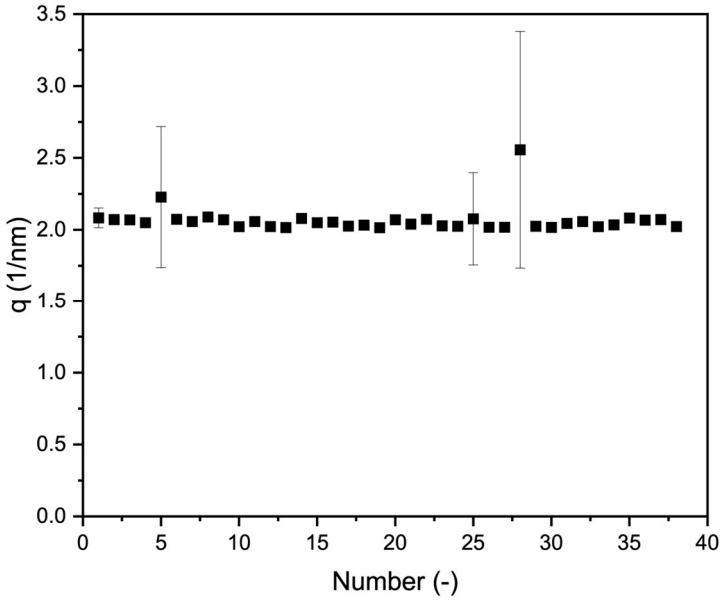


**Figure A1.** Comparison of the mean maximum q-values across all 38 datasets, along with the corresponding standard deviations.

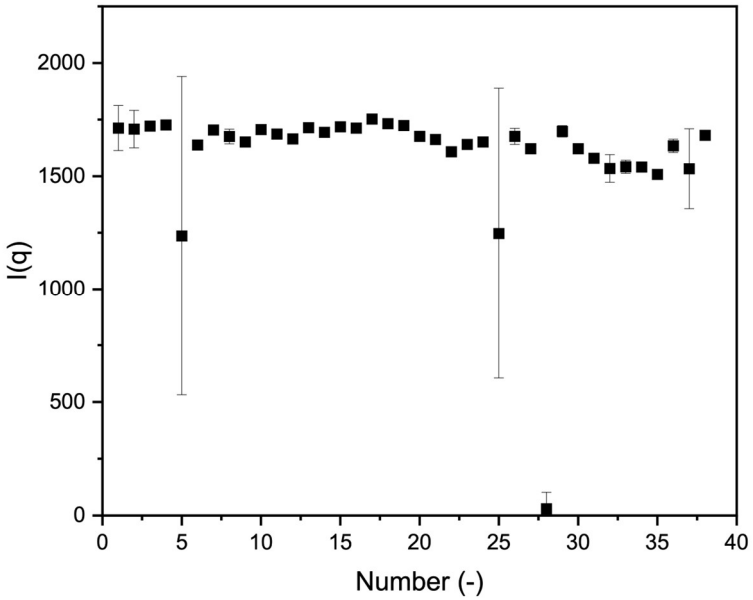


**Figure A2.** Comparison of the mean maximum I(q)-values across all 38 datasets, along with the corresponding standard deviations.

(**A**)

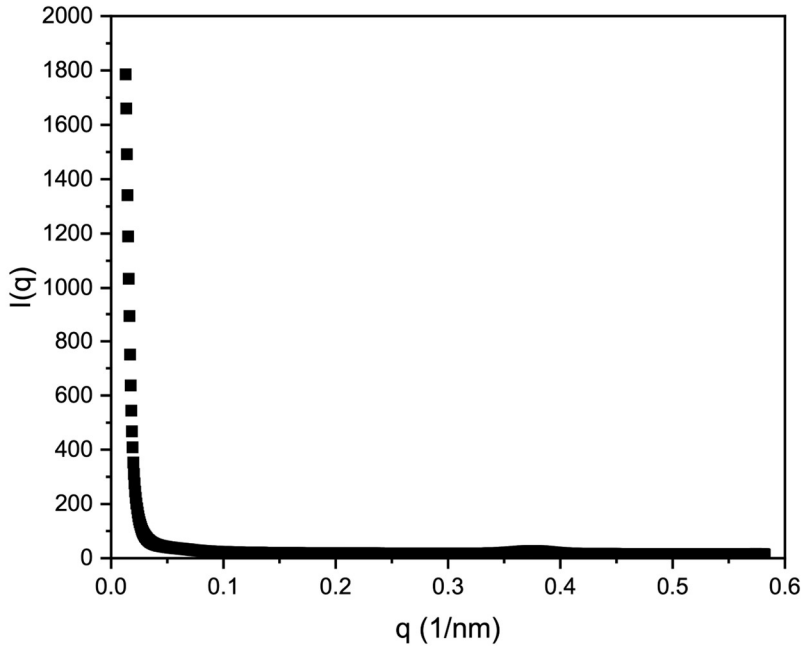


(**B**)

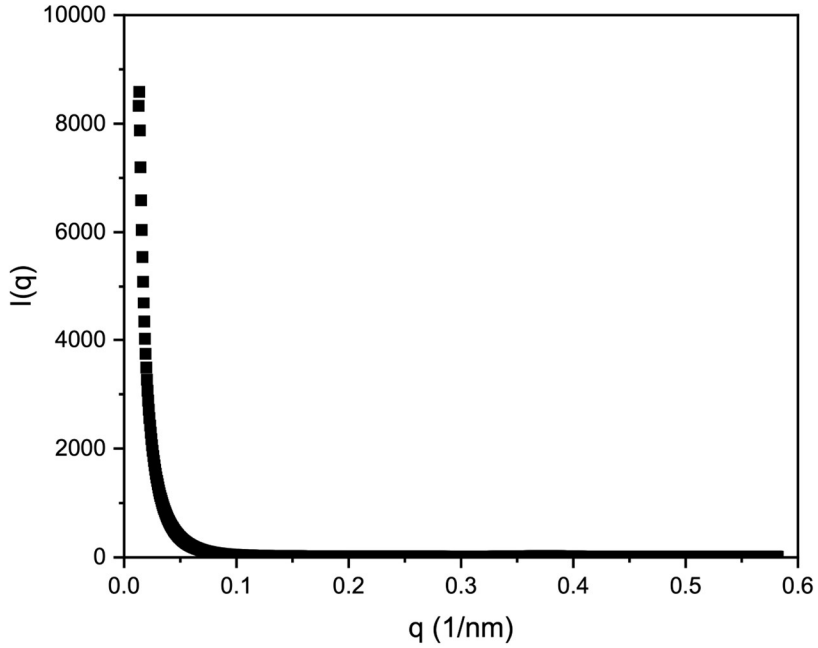


**Figure A3.** Exemplary Guinier plot of the SAXS data from Dataset (**A**) at timepoint 5 s and Dataset (**B**) at timepoint 10 min.

## *Appendix A.2. Statistical Analysis*

**Table A1.** RSM Results of Starting Point; ** indicates quadratic effect.

| | *coef.* | *std. err.* | *t* | *P* > \|*t*\| | *[0.025* | *0.975]* |
|---|---|---|---|---|---|---|
| *Intercept* | −842.9686 | 3550.179 | −0.237 | 0.818 | −8874.032 | 7188.095 |
| *A* | 426.1208 | 1757.904 | 0.242 | 0.814 | −3550.535 | 4402.776 |
| *B* | 435.4094 | 1789.391 | 0.243 | 0.813 | −3612.473 | 4483.292 |
| *C* | 569.6892 | 2366.665 | 0.241 | 0.815 | −4784.080 | 5923.458 |
| *D* | 568.1735 | 2366.364 | 0.240 | 0.816 | −4784.913 | 5921.260 |
| *E* | −570.2061 | 2366.706 | −0.241 | 0.815 | −5924.067 | 4783.654 |
| *F* | 456.3835 | 1893.237 | 0.241 | 0.815 | −3826.415 | 4739.182 |
| *A–B* | 857.0640 | 3550.097 | 0.241 | 0.815 | −7173.814 | 8887.942 |
| *A–C* | −571.4257 | 2365.252 | −0.242 | 0.815 | −5921.997 | 4779.146 |
| *A–D* | −569.4814 | 2366.945 | −0.241 | 0.815 | −5923.882 | 4784.919 |
| *A–E* | 570.8060 | 2364.412 | 0.241 | 0.815 | −4777.865 | 5919.477 |
| *A–F* | −454.3472 | 1890.490 | −0.240 | 0.815 | −4730.933 | 3822.239 |
| *B–C* | −563.3839 | 2365.556 | −0.238 | 0.817 | −5914.643 | 4787.876 |
| *B–D* | −566.8439 | 2364.165 | −0.240 | 0.816 | −5914.957 | 4781.270 |
| *B–E* | 563.4867 | 2366.356 | 0.238 | 0.817 | −4789.583 | 5916.556 |
| *B–F* | −452.8683 | 1894.253 | −0.239 | 0.816 | −4737.965 | 3832.229 |
| *C–D* | −2.2129 | 2.068 | −1.070 | 0.312 | −6.891 | 2.466 |
| *C–E* | −2.5247 | 1.962 | −1.287 | 0.230 | −6.964 | 1.914 |
| *C–F* | 2.8983 | 1.582 | 1.832 | 0.100 | −0.681 | 6.477 |
| *D–E* | 0.5874 | 2.317 | 0.253 | 0.806 | −4.655 | 5.829 |
| *D–F* | 0.2099 | 2.416 | 0.087 | 0.933 | −5.256 | 5.676 |
| *E–F* | −1.8872 | 1.001 | −1.885 | 0.092 | −4.152 | 0.377 |
| *I(A)* ** | 429.8288 | 1792.032 | 0.240 | 0.816 | −3624.030 | 4483.688 |
| *I(B)* ** | 423.7768 | 1759.641 | 0.241 | 0.815 | −3556.809 | 4404.362 |
| *I(C)* ** | 1.3066 | 2.458 | 0.532 | 0.608 | −4.255 | 6.868 |
| *I(D)* ** | −10.1404 | 3.281 | −3.090 | 0.013 | −17.563 | −2.718 |
| *I(E)* ** | 7.9543 | 3.797 | 2.095 | 0.066 | −0.636 | 16.544 |
| *I(F)* ** | 1.7173 | 4.239 | 0.405 | 0.695 | −7.873 | 11.307 |

**Table A2.** RSM Results of Slope; ** indicates quadratic effect.

| | *coef.* | *std. err.* | *t* | *P* > \|*t*\| | *[0.025* | *0.975]* |
|---|---|---|---|---|---|---|
| *Intercept* | 0.2659 | 0.167 | 1.592 | 0.155 | −0.129 | 0.661 |
| *A* | 0.0854 | 0.076 | 1.129 | 0.296 | −0.093 | 0.264 |
| *B* | −0.0914 | 0.053 | −1.716 | 0.130 | −0.217 | 0.035 |
| *C* | −0.0307 | 0.044 | −0.699 | 0.507 | −0.135 | 0.073 |
| *D* | −0.1022 | 0.082 | −1.244 | 0.254 | −0.297 | 0.092 |
| *E* | −0.0004 | 0.065 | −0.007 | 0.995 | −0.155 | 0.154 |
| *F* | 0.0381 | 0.047 | 0.819 | 0.440 | −0.072 | 0.148 |
| *A–B* | −0.2818 | 0.098 | −2.876 | 0.024 | −0.514 | −0.050 |
| *A–C* | 0.2387 | 0.081 | 2.957 | 0.021 | 0.048 | 0.430 |
| *A–D* | −0.0182 | 0.165 | −0.111 | 0.915 | −0.408 | 0.371 |
| *A–E* | −0.1685 | 0.105 | −1.598 | 0.154 | −0.418 | 0.081 |
| *A–F* | −0.1870 | 0.081 | −2.309 | 0.054 | −0.378 | 0.004 |
| *B–C* | −0.0957 | 0.091 | −1.048 | 0.329 | −0.312 | 0.120 |
| *B–D* | 0.1696 | 0.111 | 1.524 | 0.171 | −0.094 | 0.433 |
| *B–E* | 0.2347 | 0.065 | 3.613 | 0.009 | 0.081 | 0.388 |
| *B–F* | 0.0807 | 0.070 | 1.150 | 0.288 | −0.085 | 0.247 |
| *C–D* | 0.0281 | 0.085 | 0.331 | 0.751 | −0.173 | 0.229 |
| *C–E* | −0.1711 | 0.061 | −2.802 | 0.026 | −0.316 | −0.027 |
| *C–F* | −0.0116 | 0.063 | −0.184 | 0.859 | −0.160 | 0.137 |
| *D–E* | −0.0412 | 0.128 | −0.321 | 0.757 | −0.344 | 0.262 |
| *D–F* | 0.0805 | 0.066 | 1.226 | 0.260 | −0.075 | 0.236 |
| *E–F* | 0.1423 | 0.088 | 1.615 | 0.150 | −0.066 | 0.351 |
| *I(A)* ** | 0.1045 | 0.072 | 1.447 | 0.191 | −0.066 | 0.275 |
| *I(B)* ** | 0.0998 | 0.079 | 1.256 | 0.249 | −0.088 | 0.288 |
| *I(C)* ** | 0.1673 | 0.077 | 2.184 | 0.065 | −0.014 | 0.348 |
| *I(D)* ** | −0.1391 | 0.075 | −1.843 | 0.108 | −0.317 | 0.039 |
| *I(E)* ** | 0.0789 | 0.213 | 0.370 | 0.723 | −0.426 | 0.584 |
| *I(F)* ** | −0.3032 | 0.101 | −2.998 | 0.020 | −0.542 | −0.064 |

**Table A3.** RSM Results Endpoint; ** indicates quadratic effect.

| | *coef.* | *std. err.* | *t* | *P* > \|*t*\| | *[0.025* | *0.975]* |
|---|---|---|---|---|---|---|
| *Intercept* | 78.0686 | 4.665 | 16.733 | 0.000 | 67.310 | 88.827 |
| *A* | 3.3778 | 1.938 | 1.743 | 0.120 | −1.091 | 7.847 |
| *B* | −3.8613 | 2.130 | −1.812 | 0.107 | −8.774 | 1.052 |
| *C* | 4.1408 | 2.034 | 2.036 | 0.076 | −0.549 | 8.831 |
| *D* | 11.8782 | 2.081 | 5.708 | 0.000 | 7.079 | 16.677 |
| *E* | −3.1578 | 2.036 | −1.551 | 0.159 | −7.852 | 1.537 |
| *F* | −1.7741 | 1.984 | −0.894 | 0.397 | −6.349 | 2.801 |
| *A–B* | 7.0448 | 2.630 | 2.678 | 0.028 | 0.979 | 13.111 |
| *A–C* | 0.7316 | 2.487 | 0.294 | 0.776 | −5.003 | 6.466 |
| *A–D* | 0.4087 | 2.536 | 0.161 | 0.876 | −5.438 | 6.256 |
| *A–E* | 8.0901 | 2.397 | 3.375 | 0.010 | 2.563 | 13.617 |
| *A–F* | 0.3619 | 2.456 | 0.147 | 0.887 | −5.303 | 6.027 |
| *B–C* | 5.4117 | 2.519 | 2.148 | 0.064 | −0.397 | 11.221 |
| *B–D* | −0.6871 | 2.595 | −0.265 | 0.798 | −6.671 | 5.297 |
| *B–E* | −2.0634 | 2.588 | −0.797 | 0.448 | −8.030 | 3.903 |
| *B–F* | −1.3129 | 2.714 | −0.484 | 0.642 | −7.572 | 4.947 |
| *C–D* | 3.0157 | 2.466 | 1.223 | 0.256 | −2.672 | 8.703 |
| *C–E* | −5.0761 | 2.455 | −2.068 | 0.073 | −10.738 | 0.585 |
| *C–F* | 1.6900 | 2.471 | 0.684 | 0.513 | −4.009 | 7.389 |
| *D–E* | 6.2209 | 2.534 | 2.455 | 0.040 | 0.378 | 12.064 |
| *D–F* | 0.6270 | 2.617 | 0.240 | 0.817 | −5.407 | 6.661 |
| *E–F* | −0.0233 | 2.445 | −0.010 | 0.993 | −5.663 | 5.616 |
| *I(A)* ** | −2.9300 | 3.622 | −0.809 | 0.442 | −11.282 | 5.422 |
| *I(B)* ** | −6.4246 | 3.768 | −1.705 | 0.127 | −15.113 | 2.264 |
| *I(C)* ** | −13.9334 | 4.072 | −3.422 | 0.009 | −23.324 | −4.543 |
| *I(D)* ** | 6.8123 | 3.819 | 1.784 | 0.112 | −1.993 | 15.618 |
| *I(E)* ** | −4.6823 | 4.122 | −1.136 | 0.289 | −14.187 | 4.822 |
| *I(F)* ** | 2.5178 | 3.981 | 0.632 | 0.545 | −6.662 | 11.698 |

## References


1. Favela-Camacho, S.E.; Samaniego-Benítez, E.J.; Godínez-García, A.; Avilés-Arellano, L.M.; Pérez-Robles, J.F. How to decrease the agglomeration of magnetite nanoparticles and increase their stability using surface properties. *Colloids Surf. A Physicochem. Eng. Asp.* **2019**, *574*, 29–35. [CrossRef]
2. Paunovic, J.; Vucevic, D.; Radosavljevic, T.; Mandić-Rajčević, S.; Pantic, I. Iron-based nanoparticles and their potential toxicity: Focus on oxidative stress and apoptosis. *Chem. Biol. Interact.* **2020**, *316*, 108935. [CrossRef] [PubMed]
3. Fraga-García, P.; Kubbutat, P.; Brammen, M.; Schwaminger, S.; Berensmeier, S. Bare Iron Oxide Nanoparticles for Magnetic Harvesting of Microalgae: From Interaction Behavior to Process Realization. *Nanomaterials* **2018**, *8*, 292. [CrossRef] [PubMed]
4. Zhang, Y.; Liu, J.Y.; Ma, S.; Zhang, Y.J.; Zhao, X.; Zhang, X.D.; Zhang, Z.D. Synthesis of PVP-coated ultra-small Fe3O4 nanoparticles as a MRI contrast agent. *J. Mater. Sci. Mater. Med.* **2010**, *21*, 1205–1210. [CrossRef] [PubMed]
5. Cho, M.; Villanova, J.; Ines, D.M.; Chen, J.; Lee, S.S.; Xiao, Z.; Guo, X.; Dunn, J.A.; Stueber, D.D.; Decuzzi, P.; et al. Sensitive T2 MRI Contrast Agents from the Rational Design of Iron Oxide Nanoparticle Surface Coatings. *J. Phys. Chem. C* **2023**, *127*, 1057–1070. [CrossRef]
6. Zhao, Z.; Zhou, Z.; Bao, J.; Wang, Z.; Hu, J.; Chi, X.; Ni, K.; Wang, R.; Chen, X.; Chen, Z.; et al. Octapod iron oxide nanoparticles as high-performance T2 contrast agents for magnetic resonance imaging. *Nat. Commun.* **2013**, *4*, 2266. [CrossRef]
7. Ghosh, D.; Lee, Y.; Thomas, S.; Kohli, A.G.; Yun, D.S.; Belcher, A.M.; Kelly, K.A. M13-templated magnetic nanoparticles for targeted in vivo imaging of prostate cancer. *Nat. Nanotechnol.* **2012**, *7*, 677–682. [CrossRef]
8. Crezee, J.; Franken, N.A.P.; Oei, A.L. Hyperthermia-Based Anti-Cancer Treatments. *Cancers* **2021**, *13*, 1240. [CrossRef]
9. Hervault, A.; Thanh, N.T.K. Magnetic nanoparticle-based therapeutic agents for thermo-chemotherapy treatment of cancer. *Nanoscale* **2014**, *6*, 11553–11573. [CrossRef]
10. Blanco-Andujar, C.; Walter, A.; Cotin, G.; Bordeianu, C.; Mertz, D.; Felder-Flesch, D.; Begin-Colin, S. Design of iron oxide-based nanoparticles for MRI and magnetic hyperthermia. *Nanomedicine* **2016**, *11*, 1889–1910. [CrossRef]
11. Avval, Z.M.; Malekpour, L.; Raeisi, F.; Babapoor, A.; Mousavi, S.M.; Hashemi, S.A.; Salari, M. Introduction of magnetic and supermagnetic nanoparticles in new approach of targeting drug delivery and cancer therapy application. *Drug Metab. Rev.* **2020**, *52*, 157–184. [CrossRef] [PubMed]
12. Massart, R. Preparation of aqueous magnetic liquids in alkaline and acidic media. *IEEE Trans. Magn.* **1981**, *17*, 1247–1248. [CrossRef]
13. Schwaminger, S.P.; Syhr, C.; Berensmeier, S. Controlled Synthesis of Magnetic Iron Oxide Nanoparticles: Magnetite or Maghemite? *Crystals* **2020**, *10*, 214. [CrossRef]

14. Adrianzen Herrera, D.; Ashai, N.; Perez-Soler, R.; Cheng, H. Nanoparticle albumin bound-paclitaxel for treatment of advanced non-small cell lung cancer: An evaluation of the clinical evidence. *Expert. Opin. Pharmacother.* **2019**, *20*, 95–102. [CrossRef]
15. Ankamwar, B.; Lai, T.C.; Huang, J.H.; Liu, R.S.; Hsiao, M.; Chen, C.H.; Hwu, Y.K. Biocompatibility of $Fe_3O_4$ nanoparticles evaluated by in vitro cytotoxicity assays using normal, glia and breast cancer cells. *Nanotechnology* **2010**, *21*, 075102. [CrossRef] [PubMed]
16. Baskar, G.; Ravi, M.; Panda, J.J.; Khatri, A.; Dev, B.; Santosham, R.; Sathiya, S.; Babu, C.S.; Chauhan, V.S.; Rayala, S.K.; et al. Efficacy of Dipeptide-Coated Magnetic Nanoparticles in Lung Cancer Models Under Pulsed Electromagnetic Field. *Cancer Investig.* **2017**, *35*, 431–442. [CrossRef]
17. Saadat, M.; Manshadi, M.K.D.; Mohammadi, M.; Zare, M.J.; Zarei, M.; Kamali, R.; Sanati-Nezhad, A. Magnetic particle targeting for diagnosis and therapy of lung cancers. *J. Control. Release* **2020**, *328*, 776–791. [CrossRef]
18. Theodosiou, M.; Sakellis, E.; Boukos, N.; Kusigerski, V.; Kalska-Szostko, B.; Efthimiadou, E. Iron oxide nanoflowers encapsulated in thermosensitive fluorescent liposomes for hyperthermia treatment of lung adenocarcinoma. *Sci. Rep.* **2022**, *12*, 8697. [CrossRef]
19. Marcuello, C.; Chambel, L.; Rodrigues, M.S.; Ferreira, L.P.; Cruz, M.M. Magnetotactic Bacteria: Magnetism Beyond Magnetosomes. *IEEE Trans. NanoBioscience* **2018**, *17*, 555–559. [CrossRef]
20. Patsula, V.; Kosinová, L.; Lovrić, M.; Ferhatovic Hamzić, L.; Rabyk, M.; Konefal, R.; Paruzel, A.; Šlouf, M.; Herynek, V.; Gajović, S.; et al. Superparamagnetic Fe3O4 Nanoparticles: Synthesis by Thermal Decomposition of Iron(III) Glucuronate and Application in Magnetic Resonance Imaging. *ACS Appl. Mater. Interfaces* **2016**, *8*, 7238–7247. [CrossRef]
21. Nam, N.H.; Luong, N.H. Chapter 7—Nanoparticles: Synthesis and applications. In *Materials for Biomedical Engineering*; Grumezescu, V., Grumezescu, A.M., Eds.; Elsevier: Amsterdam, The Netherlands, 2019; pp. 211–240.
22. Dudchenko, N.; Pawar, S.; Perelshtein, I.; Fixler, D. Magnetite Nanoparticles: Synthesis and Applications in Optics and Nanophotonics. *Materials* **2022**, *15*, 2601. [CrossRef] [PubMed]
23. Unni, M.; Uhl, A.M.; Savliwala, S.; Savitzky, B.H.; Dhavalikar, R.; Garraud, N.; Arnold, D.P.; Kourkoutis, L.F.; Andrew, J.S.; Rinaldi, C. Thermal Decomposition Synthesis of Iron Oxide Nanoparticles with Diminished Magnetic Dead Layer by Controlled Addition of Oxygen. *ACS Nano* **2017**, *11*, 2284–2303. [CrossRef] [PubMed]
24. Darr, J.A.; Zhang, J.; Makwana, N.M.; Weng, X. Continuous Hydrothermal Synthesis of Inorganic Nanoparticles: Applications and Future Directions. *Chem. Rev.* **2017**, *117*, 11125–11238. [CrossRef] [PubMed]
25. Jafari Eskandari, M.; Hasanzadeh, I. Size-controlled synthesis of Fe3O4 magnetic nanoparticles via an alternating magnetic field and ultrasonic-assisted chemical co-precipitation. *Mater. Sci. Eng. B* **2021**, *266*, 115050. [CrossRef]
26. Besenhard, M.O.; LaGrow, A.P.; Hodzic, A.; Kriechbaum, M.; Panariello, L.; Bais, G.; Loizou, K.; Damilos, S.; Margarida Cruz, M.; Thanh, N.T.K.; et al. Co-precipitation synthesis of stable iron oxide nanoparticles with NaOH: New insights and continuous production via flow chemistry. *Chem. Eng. J.* **2020**, *399*, 125740. [CrossRef]
27. Mourdikoudis, S.; Pallares, R.M.; Thanh, N.T.K. Characterization techniques for nanoparticles: Comparison and complementarity upon studying nanoparticle properties. *Nanoscale* **2018**, *10*, 12871–12934. [CrossRef]
28. Gommes, C.J. Ostwald ripening of confined nanoparticles: Chemomechanical coupling in nanopores. *Nanoscale* **2019**, *11*, 7386–7393. [CrossRef]
29. Eigenfeld, M.; Wittmann, L.; Kerpes, R.; Schwaminger, S.P.; Becker, T. Studying the impact of cell age on the yeast growth behaviour of *Saccharomyces pastorianus var. carlsbergensis* by magnetic separation. *Biotechnol. J.* **2023**, *18*, 2200610. [CrossRef] [PubMed]
30. Turrina, C.; Berensmeier, S.; Schwaminger, S.P. Bare Iron Oxide Nanoparticles as Drug Delivery Carrier for the Short Cationic Peptide Lasioglossin. *Pharmaceuticals* **2021**, *14*, 405. [CrossRef]
31. Mao, Y.; Li, Y.; Guo, Z.; Chen, B.; Qin, Z.; Zhang, Z.; Sun, J.; Gu, N. The coprecipitation formation study of iron oxide nanoparticles with the assist of a gas/liquid mixed phase fluidic reactor. *Colloids Surf. A Physicochem. Eng. Asp.* **2022**, *647*, 129107. [CrossRef]
32. Li, T.; Senesi, A.J.; Lee, B. Small Angle X-ray Scattering for Nanoparticle Research. *Chem. Rev.* **2016**, *116*, 11128–11180. [CrossRef] [PubMed]
33. Haas, S.; Sun, X.; Conceicao, A.L.C.; Horbach, J.; Pfeffer, S. The new small-angle X-ray scattering beamline for materials research at PETRA III: SAXSMAT beamline P62. *J. Synchrotron Radiat.* **2023**, *6*, 1156–1167. [CrossRef] [PubMed]
34. Cleveland, W.S.; Devlin, S.J. Locally Weighted Regression: An Approach to Regression Analysis by Local Fitting. *J. Am. Stat. Assoc.* **1988**, *83*, 596–610. [CrossRef]
35. Schmid, M.; Rath, D.; Diebold, U. Why and How Savitzky–Golay Filters Should Be Replaced. *ACS Meas. Sci. Au* **2022**, *2*, 185–196. [CrossRef]
36. Ravikumar, C. Unveiling the formation mechanism of polydisperse iron oxide nanoparticles in coprecipitation route. *J. Cryst. Growth* **2023**, *624*, 127419. [CrossRef]
37. Pearce, A.K.; Wilks, T.R.; Arno, M.C.; O'Reilly, R.K. Synthesis and applications of anisotropic nanoparticles with precisely defined dimensions. *Nat. Rev. Chem.* **2021**, *5*, 21–45. [CrossRef]
38. Roth, H.C.; Schwaminger, S.P.; Peng, F.; Berensmeier, S. Immobilization of Cellulase on Magnetic Nanocarriers. *ChemistryOpen* **2016**, *5*, 183–187. [CrossRef] [PubMed]
39. Winsett, J.; Moilanen, A.; Paudel, K.; Kamali, S.; Ding, K.; Cribb, W.; Seifu, D.; Neupane, S. Quantitative determination of magnetite and maghemite in iron oxide nanoparticles using Mössbauer spectroscopy. *SN Appl. Sci.* **2019**, *1*, 1636. [CrossRef]

40. Suharyana; Febriani, R.R.; Prasetya, N.P.; Utari; Wibowo, N.A.; Suharno; Supriyanto, A.; Ramelan, A.H.; Purnama, B. Sodium-hydroxide molarities influence the structural and magnetic properties of strontium-substituted cobalt ferrite nanoparticles produced via co-precipitation. *Kuwait J. Sci.* **2023**, *50*, 575–579. [CrossRef]
41. Siregar, N.; Indrayana, I.P.T.; Suharyadi, E.; Kato, T.; Iwata, S. Effect of Synthesis Temperature and NaOH Concentration on Microstructural and Magnetic Properties of Mn0.5Zn0.5Fe2O4 Nanoparticles. *IOP Conf. Ser. Mater. Sci. Eng.* **2017**, *202*, 012048. [CrossRef]
42. Karaagac, O.; Köçkar, H. Effect of Synthesis Parameters on the Properties of Superparamagnetic Iron Oxide Nanoparticles. *J. Supercond. Nov. Magn.* **2012**, *25*, 2777–2781. [CrossRef]
43. Alibeigi, S.; Vaezi, M.R. Phase Transformation of Iron Oxide Nanoparticles by Varying the Molar Ratio of $Fe^{2+}$:$Fe^{3+}$. *Chem. Eng. Technol.* **2008**, *31*, 1591–1596. [CrossRef]
44. Lu, A.-H.; Salabas, E.L.; Schüth, F. Magnetic Nanoparticles: Synthesis, Protection, Functionalization, and Application. *Angew. Chem. Int. Ed.* **2007**, *46*, 1222–1244. [CrossRef] [PubMed]
45. Qu, Y.; Yang, H.; Yang, N.; Fan, Y.; Zhu, H.; Zou, G. The effect of reaction temperature on the particle size, structure and magnetic properties of coprecipitated CoFe2O4 nanoparticles. *Mater. Lett.* **2006**, *60*, 3548–3552. [CrossRef]
46. Wicaksono, S.T.; Wahfiudin, A.; Pramata, A.D.; Sagadevan, S. Effect of Fe (III)/Fe (II) cation molar ratio variation on magnetite Fe3O4 nanoparticles synthesized from natural iron sand by co-precipitation method. *MRS Adv.* **2024**. [CrossRef]
47. Mona, L.P.; Songca, S.P.; Ajibade, P.A. Effects of Temperature and Precursor Concentration on the Morphological and Optical Properties of Iron Oxide Nanoparticles. *Chem. Afr.* **2024**, *7*, 4581–4591. [CrossRef]